

Inverse-Designed Photonic Crystal Devices for Optical Beam Steering

Dries Vercruyssen¹, Neil V. Sapiro¹, Ki Youl Yang¹, and Jelena Vučković¹

¹E. L. Ginzton Laboratory, Stanford University, Stanford, CA, USA.

The ability of photonic crystal waveguides (PCWs) to confine and slow down light makes them an effective component to enhance the performance of many photonic devices, such as optical modulators, optical sensors and optical phased arrays (OPAs). However, the integration of PCWs in photonic applications comes with various design challenges, most notably, engineering the PCW mode dispersion and efficiently coupling to the modes of the PCW. Here, we solve these challenges through the use of inverse design methodologies. The dispersion relation of even and odd mode PCWs are engineered for a group index of 25 over a bandwidth of 20 nm and 12 nm, respectively. For both PCW designs, we create strip waveguide couplers, as well as free space grating couplers. The transmission of optical delay devices constructed with the strip waveguide converters are experimentally characterized and, using the PCW grating couplers, the group index of both PCWs is measured. Finally, radiative losses are introduced to our PCW designs while maintaining the dispersion relation of the original PCW. With these loss and dispersion engineered PCWs, alongside the strip waveguide couplers, we construct OPAs with different radiative strength. The OPAs are experimentally characterized and shown to steer a light beam up to 20° in a 20 nm bandwidth. The devices in this work illustrate how inverse design methods can enable the use of PCWs in future LiDAR systems, optical communication, and sensing applications.

Photonic crystal waveguides (PCWs), constructed by a defect line in a photonic crystal lattice, possess remarkably tuneable optical modes, whose properties can be engineered for various photonic applications. Non-linear photonic devices or emission systems can achieve increased efficiency and reduced device size by relying on the ability of the PCW to spatially compress optical energy and enhance light matter-interaction [1–6]. Modulators and sensors use slow light PCWs for their high phase-velocity sensitivity to the refractive index of the waveguide or surrounding medium [7–14]. Recently, slow light PCWs were shown to be an effective basis for optical phased arrays (OPAs), providing improvements in their beam steering capabilities [15–18]. The wavelength-dependent steering sensitivity of the OPA depends on the dispersion relation of the waveguides that feed the OPA antennas. The smaller the group velocity of the waveguides, the larger the beam deflection by a change in wavelength [19–26]. Therefore, a slow light PCW can be used to increase the OPA scanning range while reducing its operating bandwidth.

PCW design is complicated and forms a hurdle in its adoption, despite the many benefits. The challenge is twofold: first, the photonic crystal defect line needs to be modified to match the desired dispersion relation of the application, and second, mode converters need to be constructed to couple to the PCW mode efficiently. Classical dispersion engineering methods typically vary a few geometric parameters, such as the position or radius of lattice holes around the defect line, to optimize the dispersion relation [27–29]. In contrast, inverse design can optimize arbitrary shapes by relying on adjoint methods to manage the large number of degrees of freedom of these design geometries [16, 30]. This has enabled compact and highly efficient photonic devices, and makes inverse design highly suited for the dispersion optimization of lattice defect lines [31–36]. Additionally, poor modal over-

lap and group-index mismatch results in high insertion losses into the PCW, which need to be mitigated by coupling devices. While tapering of the lattice can achieve high coupling efficiency for unaltered defects line, this classical photonic solution becomes difficult for a defect line with modifications [29]. Inverse design steps away from this simple, but limited approach, and leverages a much larger design space to construct couplers to high efficiency couplers in the intended bandwidth [35, 36].

In this work, we demonstrate the use of inverse design for PCWs-based photonics systems to construct a compact, slow light OPA with a wide steering angle achievable with a small operating bandwidth. First, we illustrate how inverse design can be used for dispersion engineering by creating slow light PCWs for both even and odd optical modes. For both modes, couplers are designed for conversion from a strip waveguide, as well as free space grating couplers. We measure the coupling efficiency and waveguide losses of slow light devices constructed with these PCWs and strip waveguide couplers (Fig. 1a). Additionally, the photonic crystal grating couplers are utilized to characterize the dispersion of the optimized waveguides. Finally, we use inverse design to modify the PCW and intentionally introduce radiative losses. Using inverse design, we show that the radiation can be optimized to a target value, while keeping the dispersion relation unaltered. Three OPA designs, each with different radiative strengths are experimentally demonstrated to sweep a 20° angle over a 20 nm operating bandwidth. This is in stark contrast to the steering specification of OPAs based on strip waveguides, which sweep about 15° in 100 nm bandwidth [26].

Inverse design dispersion engineering. The two design problems for the slow light systems are illustrated in Fig. 1b, where a strip waveguide couples to a W1 type

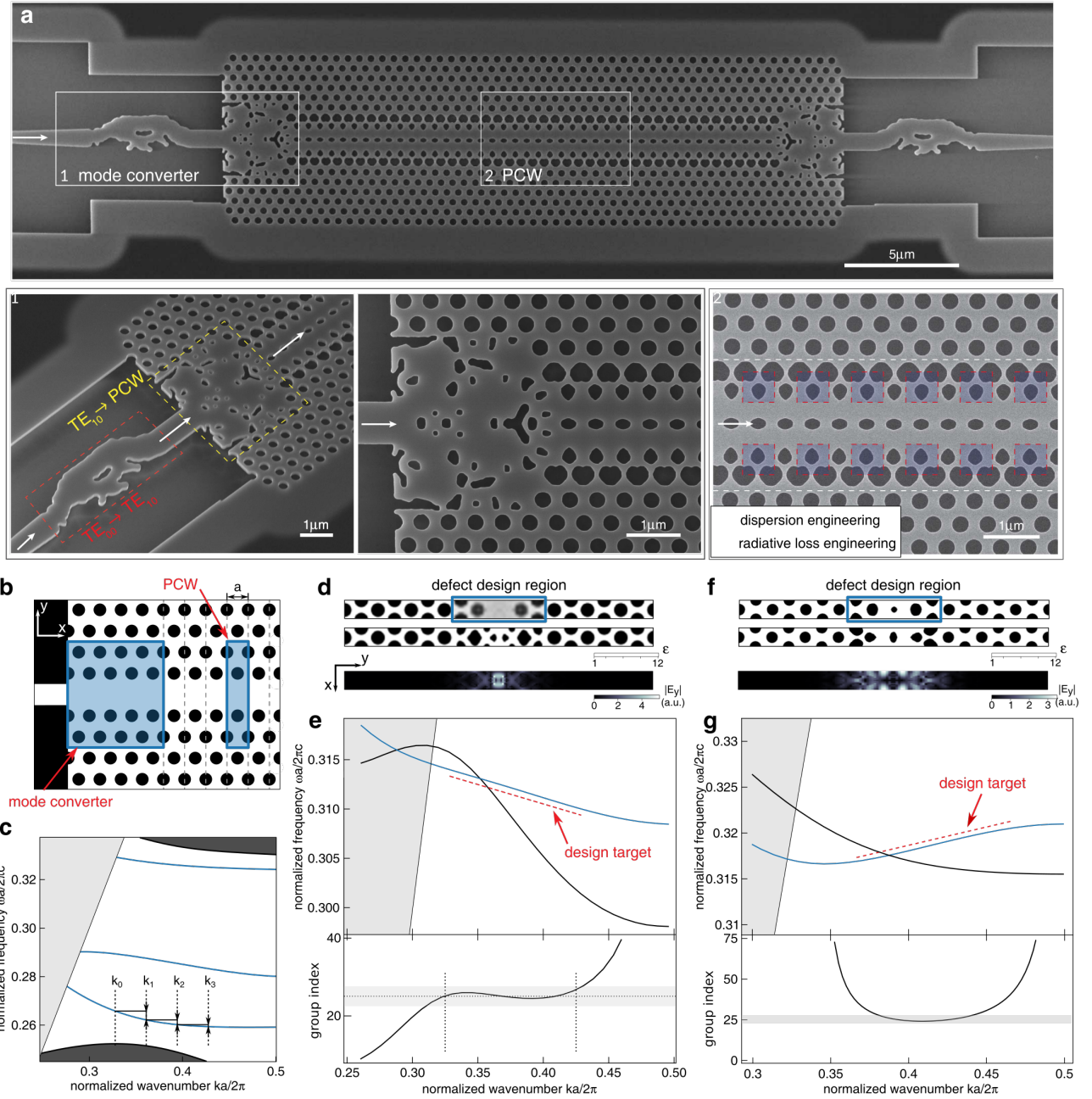


FIG. 1. **Dispersion engineering with inverse design** (a) SEM micrograph of an inverse designed PCW slow light device. Insets: a detail image of a two-stage mode converter is shown in panel 1. Panel 2 shows the inverse designed PCW with the design regions for dispersion engineering in red and radiative loss engineering in blue. (b) Design regions in a slow light device. The right blue area: the design region of the photonic crystal with period a ; the left blue region indicates the design region for the strip-to-PCW mode coupler. (c) Band diagram of photonic crystal defect line. On the bottom guided mode, the frequency difference for four wavenumber is indicated. (d,f) Initial (top), and final (middle) permittivity and $|E_y|$ fields profile (bottom) for an even mode (d) and odd mode (f). (e,g) Top: dispersion relation of the initial (black) and final (blue) PCW structure for the even (e) and odd (g) mode. The dashed line indicated the target slope. The gray area is the light cone. Bottom: group index of the final structure. The gray area indicates the $\pm 10\%$ deviation around the center group index.

PCW. We first optimize the PCW for linear dispersion by altering a region around the defect line, which encompasses two rows on either side of the waveguide (right box in Fig. 1b). Once the waveguide is optimized, cou-

plers are designed, for which we allocate a design region encompassing several periods (left box in Fig. 1b).

We demonstrate two PCWs designs: an even mode design with a negative slope dispersion relation, and an odd

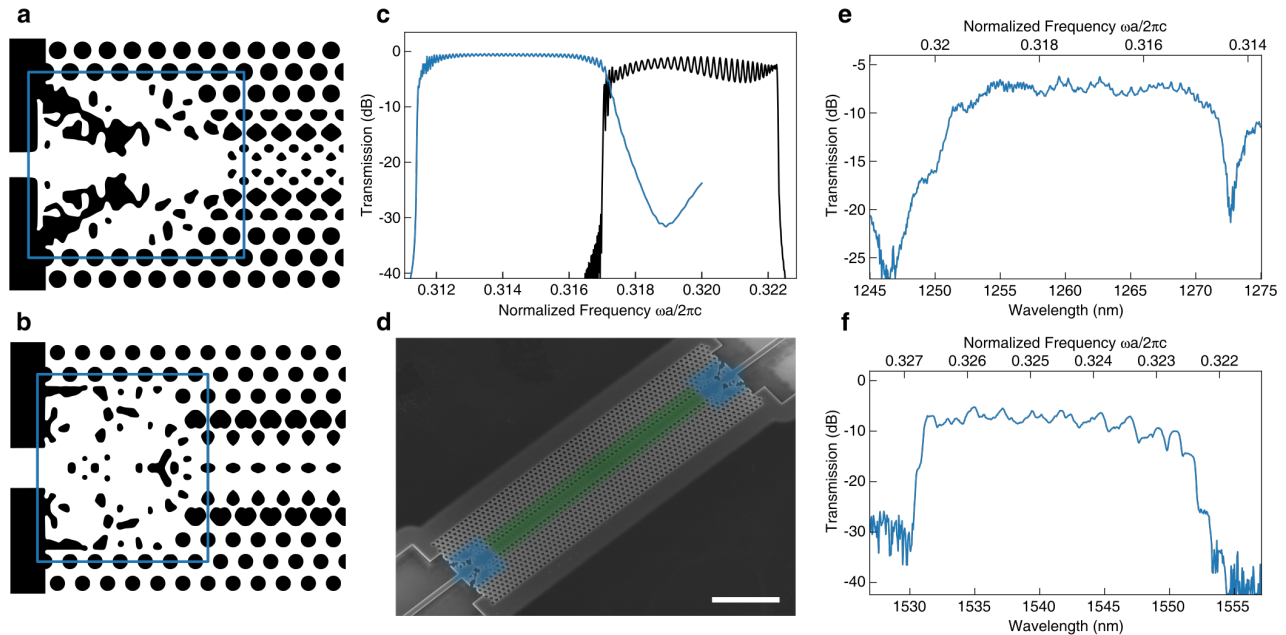


FIG. 2. **Slow light waveguide coupler** (a,b) Final optimized coupler design for the even and odd mode, respectively. The blue rectangle indicates the design region. (c) Simulated mode coupling spectra for the even (blue) and odd (black) mode couplers. (d) Micrograph of a $20\ \mu\text{m}$ long delay system (bar: $5\ \mu\text{m}$). (e,f) transmission spectrum through a $60\ \mu\text{m}$ long delay system based on an even and odd mode, respectively. The transmission analysis showed the inverse-designed coupler has -3.4 dB and -4.5 dB average insertion loss with even and odd mode, respectively (Suppl. Info).

mode for which we force the dispersion relation to have a positive slope. For both the even and odd PCWs, the dispersion relation was optimized for a target group index of 25. To achieve this, our inverse design method aims to equalize frequency difference for a series wavenumbers, k_i , to a target difference, which matches this desired group index. An example for a W1 defect line is shown in Fig. 1c using four wavenumber values. We optimized two PCWs one for an even mode with a target group index of 25 with a negative slope, and a second one for a odd mode with a target group index of 25 with a positive slope. The two designs are made in $220\ \text{nm}$ thick silicon surrounded by air. The initial structure for the even mode PCW is shown in Fig. 1d. This unit cell has a center design region with permittivity values between that of the waveguide and background cladding and is derived from a W1 defect line. The design's operating wavelength is aimed to be around $1300\ \text{nm}$; we therefore choose the lattice constant of the photonic crystal, a , to be $400\ \text{nm}$. The dispersion relation of the initial structure is shown in Fig. 1e. After optimization, the final structure (middle Fig. 1c) has a dispersion that is linear in the $k = [0.325, 0.425]$ design interval (blue curve Fig. 1d). The PCW's group index based on this curve is shown in the bottom graph of Fig. 1e. The average group index within the design interval is 25.14. Considering a 10% margin of error (grey area in bottom graph Fig. 1e), the wavenumber interval can be extended to $[0.31\frac{2\pi}{a}, 0.43\frac{2\pi}{a}]$ resulting in a normalized bandwidth group index prod-

uct, NBGP, of 0.38 [37].

The odd mode is optimized in a similar fashion. However, here, we chose to start from the defect line shown in Fig 1f. The design was aimed for operation around $1550\ \text{nm}$ and thus has a larger lattice constant, i.e. $500\ \text{nm}$. The final optimized structure (middle graph of Fig. 1f) shows an upward curve with a slope matching the target group index of 25 (Fig. 1g). Allowing for 10% deviation, the waveguide has an operation k -interval of $[0.38, 0.45]$, a center group index of 26.8 and a NBGP product of 0.22.

Slow light system design and measurements. Coupling to photonic crystal waveguides from a conventional strip or rib waveguide often results in low efficiency due to low modal field overlap and group index mismatch. While this can be mitigated by tapering, these solutions are particularly difficult for photonic crystal waveguide that deviate from a simple defect line bases on a hole lattice. For both PCW designs, we created mode couplers using inverse design methods [36, 38]. Fig. 2a shows the final design for the even slow light mode for the operating wavelength interval $\frac{\omega a}{2\pi c} = [0.309, 0.314]$. The device couples the TE₀ mode from the $400\ \text{nm}$ wide strip waveguide on the left to the slow light mode. The design region, which the optimization can alter, is indicated by the blue rectangle. Similarly, we designed a coupler for the odd mode (Fig. 2 (b)) with the operating wavelength interval $\frac{\omega a}{2\pi c} = [0.322, 0.326]$. Since the slow

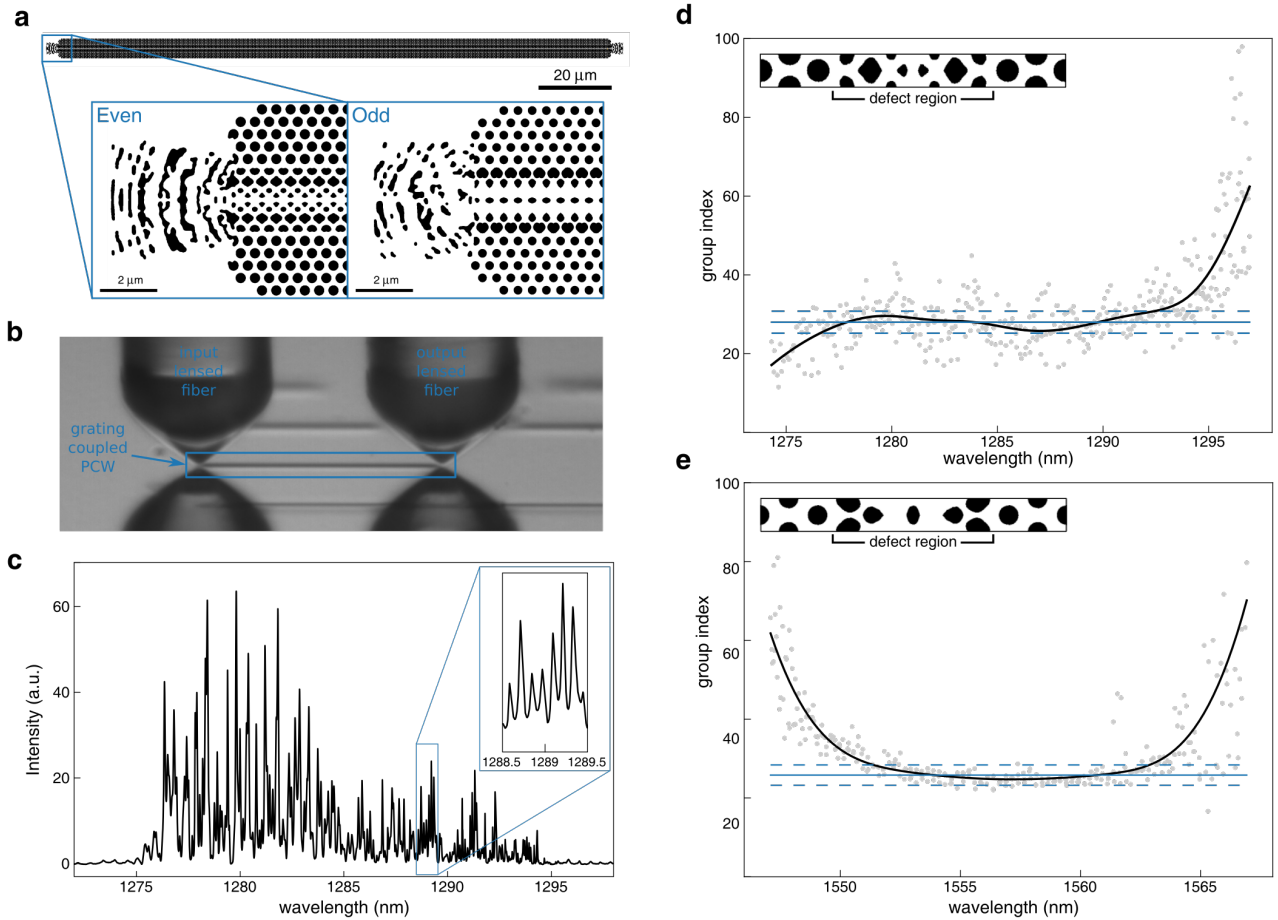


FIG. 3. **Dispersion measurement** (a) Free space coupled slow light waveguide. The insets show the inverse designed free space couplers for the even and odd mode. (b) Microscope image of the measurement setup using lensed fibers for vertical coupling. (c) Transmission spectrum of an even mode slow light waveguide through the PCW grating couplers. (d, e) Group index based on the free spectral range measurement from a transmission measurement through an even (d) and odd (e) mode. The black curve is fit though based on the grey measurement points. The solid blue line indicates the average group index. The dashed blue lines indicate a 10% deviation from the average.

light mode is odd the input mode was here was chosen to be TE₁ mode. As such the symmetry of the input and output mode symmetry is maintained which gives results in a symmetric design. A coupler, which couples from the TE₀ to odd PCW can also be created with inverse design (Suppl. Info.); however, here we opted for a combination of a TE₀-to-TE₁ mode converter and a TE₁-to-PCW couplers.

Relying on these couplers, we can construct photonic delay devices with various photonics crystal waveguide lengths. The transmission spectra for 20 μm long slow light odd and even modes waveguides were simulated using FDTD simulations (Fig 2c). Clear transmission windows for the optimised modes can be seen for both devices. Slow light waveguide devices of different length were fabricated using 220 nm thick silicon-on-insulator wafers using ebeam lithography (See methods). An SEM micrograph of a 20 μm long suspended device can be seen in Fig. 2d. The transmission spectrum of a 40 μm long,

even mode device (Fig. 2e) shows a transmission window around 1252–1272 nm, which plateaus around 7.6 dB. Devices with different PCW length were fabricated to characterise the insertion and waveguide losses. The transmission analysis showed that the even mode PCWs have -22 dB mm^{-1} losses and that the coupler has an average -3.4 dB insertion loss (Suppl. Info.). Delay devices for the odd mode we also constructed with an additional inverse designed TE₀-to-TE₁ converter at the in- and output (Suppl. Info.). The transmission spectrum for the 40 μm long device has a transmission window at 1532–1552 nm (Fig. 2f). The transmission analysis for devices with different length showed an -10 dB mm^{-1} loss for the PCW and a -4.5 dB average insertion loss for the coupler. The significantly lower losses for the odd mode compared to the even mode is to be expected from the designs and field profiles in Fig. 1d and f. The even mode design has more small features at the center of the defect line, where the field intensity is

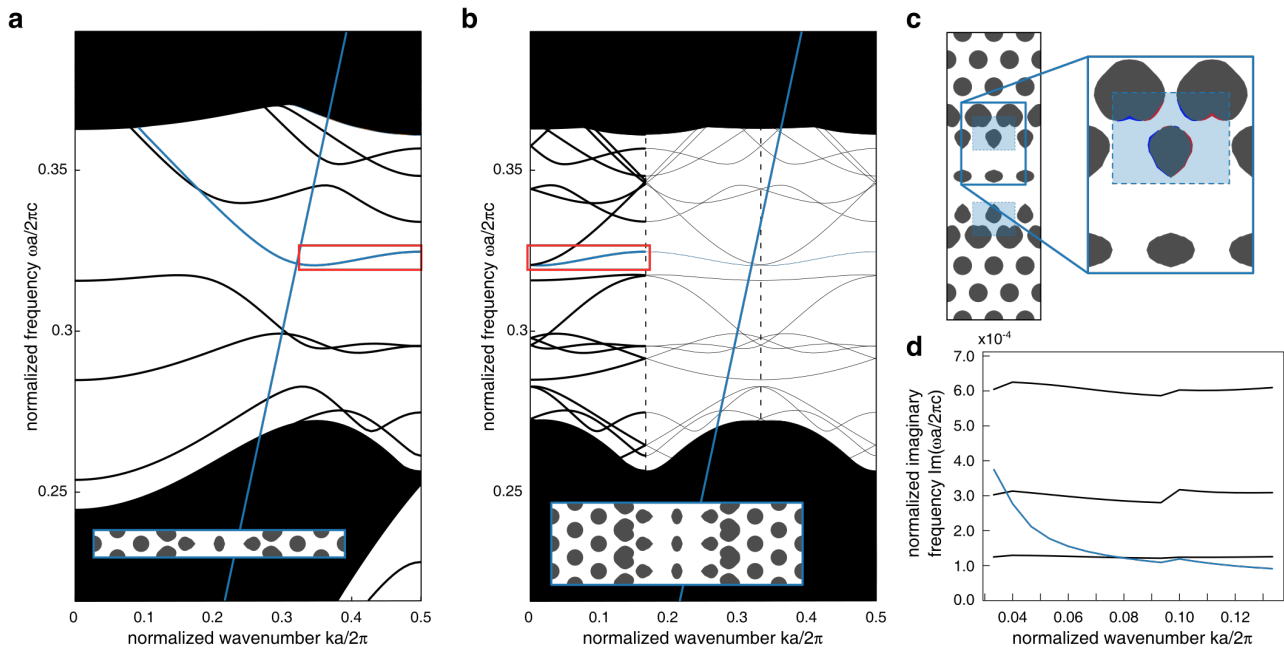


FIG. 4. **Radiative loss design** (a) full band diagram for an odd mode PCW indicated in the inset. (b) Band diagram for radiative odd mode PCW indicated in the inset (c) optimized radiative odd mode PCW. The detail image of the center indicated where material was removed (red) and added (blue) during the optimization. (d) Normalized imaginary frequency spectrum for randomly perturbed photonic crystal structure in blue, and optimized spectra in black for a target normalized imaginary frequency of 1.25×10^{-4} , 3.0×10^{-4} and 6.0×10^{-4}

high as shown by the mode fields in Fig. 1d. Fabrication errors and etch surface roughness, which are the primary loss causes, therefore impact the even mode design more than the odd mode, resulting in more losses.

Dispersion measurements. The dispersion of a waveguide can be derived from the free spectral range, FSR, of a Fabry-Perot resonator constructed with the waveguide. Such resonator can be made by edge terminating waveguide on each side; however, edge termination suffers from low coupling efficiency, especially for a high group index. Moreover, to measure the dispersion of the odd mode a higher order Gaussian beam would need to be used, which convolutes the measuring setup. Instead of using edge coupling for this measurement, we rely on inverse designed free space grating couplers, which couple directly to the PCW mode and form a low-Q Fabry-Perot resonator. Fig. 3a shows a $200 \mu\text{m}$ Fabry-Perot resonator and the inverse designed gratings couplers for the even and odd mode. For the odd mode, the input Gaussian and output mode break symmetry, which result in the asymmetric design. More information on the grating couplers can be found in the Suppl. Info.

The measurement set-up uses lensed fibers to create a $2 \mu\text{m}$ spot on the grating couplers (Fig. 3b). A transmission spectrum for an even mode Fabry-Perot resonator can be seen in Fig. 3c and shows a dense fringe pattern. The group index derived from the local FSR of the transmission spectra for three resonators,

for both the even and odd mode is plotted on Fig. 3d and e, respectively. An univariate spline fit through the points (black curve) matches the simulated results in Fig. 1e and g. Based on the fit, the group index of the even mode plateaus at 27.98 in a 1277 nm to 1293 nm $\pm 10\%$ -error spectral window, resulting in a NBGP of 0.34. The odd mode waveguide has an average group index of 25.83 in a 1552 nm to 1563 nm window, and thus has an NBGP of 0.19.

Radiative loss engineering. The flat dispersion curve makes slow light waveguides an interesting basis for OPA architectures, because a small change in wavelength translates to a large change in the wavevector of the PCW mode. Combined with a periodic perturbation to radiate out light, these waveguides can make OPAs with a large steering angle in a small operating bandwidth. However, the slow light dispersion relation is sensitive to the small alteration in the structures, and so creating a periodic perturbation which does not alter the dispersion relation is challenging. We therefore rely on inverse design to engineer radiation in the slow light waveguide while maintaining the dispersion relation. The objective function for the inverse design optimization consists of two terms. The first term aims to push the imaginary part of the frequency to our target value, which will result in the radiative losses we desire. The second term penalizes any deviation from the original dispersion relation. The objective thus relies on both the real and imaginary compo-

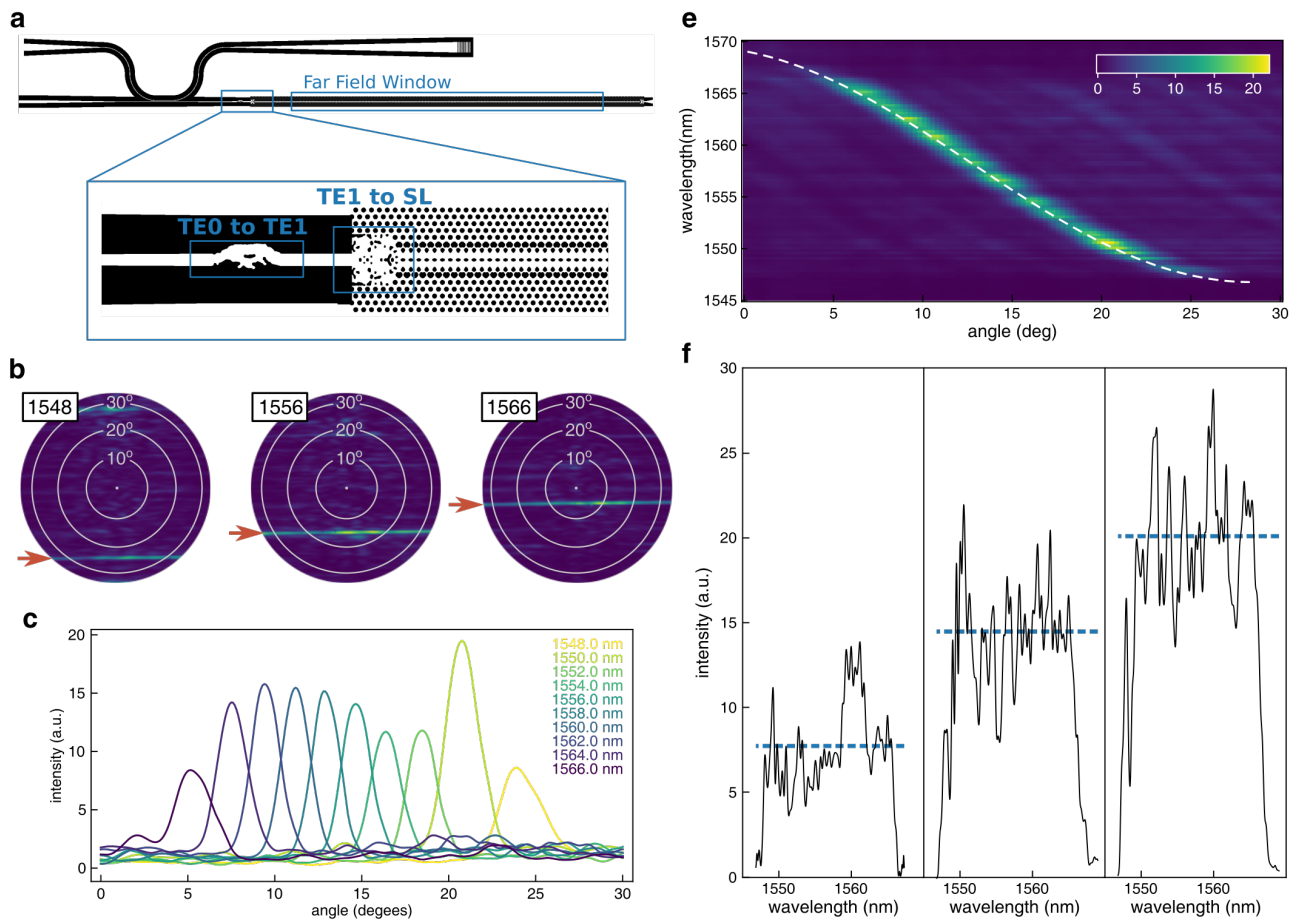


FIG. 5. **Inverse designed slow light OPA** (a) measurement circuit for the OPA. The detail illustration shows of strip-waveguide to the OPA PCW. (b) Back focal plane measurements of the far field window indicated in (a) for three wavelengths. (c) Angular spectrum for different wavelengths. (e) OPA radiation intensity heatmap in function of angle and wavelength. The dashed white line indicated where the intensity is sampled for the intensity spectrum in panel f. (f) Intensity spectra for three OPAs designed with different target imaginary frequency. The blue line indicates the average radiation intensity in the radiation window.

ment of a band calculation. For the band calculation, we use the guided mode expansion software, Legume, which we incorporated into the SPINS inverse design framework [39, 40].

We choose the odd mode waveguide as the basis for our radiation optimization. Light scattered from a defect in the slow light waveguide was seen to radiate out primarily light polarized in the x-direction. As such symmetric defects in the even mode emit quadrupole radiation pattern, while the odd mode tend to radiated in a dipole like pattern. (Suppl. Info.) The full band diagram of the odd mode is shown in Fig. 4a. As is typical for slow light waveguides the optimized band region (red rectangle) is located under the light line, so as to avoid radiative losses. For the OPA, we want to introduce radiative losses, as such we want to move the band into the light cone. This can be done by breaking the original periodicity and considering a larger period. We chose to work with a new unit cell that is three times the original

unit cell (inset Fig. 4b), and make small modification to this larger unit cell. The band diagram of the three period unit cell, which resembles the original band diagram folded in three, is now located in the light cone (Fig. 4b) The radiative losses of the mode will depend on the extent of modification. Since OPAs are typically millimeters to centimeters in length, we aimed for low radiative losses. Modifications therefore will be small, which can pose a problem in fabrication. We therefore limit the design area to the first two rows of the defect line where fields are less intense compared to the center of the waveguide. This will result in larger modifications to achieve the target losses. The design area is indicated in the inset in Fig. 4c. Finally, we make sure that the alterations are symmetric in the x-direction. Material removed on one side of the unit cell will be accompanied by adding material on the other side (Fig. 4b). This aids the dispersion optimization, since the overall material of the unit cell is not altered much by this type of alteration.

The radiative losses of three optimized devices with the target normalized imaginary frequencies of 1.25×10^{-4} , 3.0×10^{-4} and 6.0×10^{-4} , are shown in Fig. 4d. The losses for a waveguide with a random alteration, used as initial condition, is shown in blue. After optimization, the imaginary frequency over the k-space is flattened around the target value.

Beam Steering. With the inverse designed loss and dispersion engineered PCWs and couplers, we can construct a slow light OPA. The OPA and the photonic test circuit is shown in Fig. 5a. Light is coupled to the bottom waveguide on the left via an edge coupling setup and first sent to a directional coupler, which picks off some power to normalize the measurement. The transmitted light passes through a TE₀-to-TE₁ mode converter and subsequently goes to the inverse designed OPA. The OPA is constructed with the odd mode coupler, followed by twenty periods of the non-radiative odd mode PCW, after which the PCW transitions to the radiative PCWs designs. To minimize reflections the waveguide is terminated by the coupler and a taper. We evaluate the direction and intensity of the out-coupled light with a back-focal-plane (BFP) microscope (Suppl. Info.). A rectangular aperture in the bright field image plane of the BFP set-up filters out only light emitted by the OPA-waveguide (far field window in Fig. 5a). Back-focal-plane images at three different wavelengths are shown in Fig. 5b. Since only one waveguide is measured, rather than an array, the radiated light is only confined in the x-direction and not in the y-direction. The BFPs thus show a line, rather than a point, as can be seen in the BFP measurements of the OPA for 1548 nm, which emits around $\theta_x = 24^\circ$ (Fig. 5b). As the wavelength increases, the steering angle decreases, reaching $\theta_x = 5^\circ$ at 1566 nm. Angular intensity spectra can be made by integrating along the θ_y direction (Fig. 5c). The heat map constructed with these spectra shows the radiation intensity in function of θ_x and the wavelength (Fig. 5e). The dotted line fits the maximums of the angular spectra. As expected, this curve corresponds to the dispersion relation shown in Fig. 4b. A clear signal can be seen in the 1547–1567 nm wavelength interval, in which the beam is swept from $\theta_x = 25^\circ$ to $\theta_x = 5^\circ$. The intensity sampled along the fitted steering curve is shown in the middle panel of Fig 5f. On the left and right panel, the same analysis is shown for an OPA designed for the target imaginary value of 1.25×10^{-4} and 6×10^{-4} , respectively. The overall power in all three measurement was normalized to the power picked off by the direction coupler and coupled out by the grating coupler, so as to allow the comparison (Fig 5a). The average intensity, indicated by a blue dashed line, mirrors the increasing radiation power expected from the radiation losses shown in Fig 4d. The radiation intensity in function of wavelength and angle for all three OPAs can be found in the Suppl. Info.

Conclusion In conclusion, we have demonstrated the use of inverse design methods to tackle many of the design challenges associated with photonic crystal circuits – in particular in the context of on chip beam steering. Inverse design was shown to be effective in optimizing photonic crystal defect lines to match a target dispersion relation, as well as in creating couplers to the PCW modes. The versatility of this design method allows us to not only make PCW coupler to strip waveguides, but also to make grating couplers which can couple directly the PCW. These grating couplers enable us to create PCW Fabry–Pérot resonators with which we experimentally verified the group index spectra. Furthermore, we showed that the radiative losses can be added to the dispersion optimization problem. Relying on these loss and dispersion engineered waveguide designs, we constructed three OPAs with different radiative strength. A steering range of 20° in a 1547–1567 nm wavelength interval was experimentally verified. These inverse designed slow light OPAs represent a significant improvement in both steering range and operating bandwidth as compared to conventional OPAs based on silicon strip waveguides, which steer around 15° in a 100 nm bandwidth. Moreover, inverse design was shown to be highly effective in tackling the multitude of design challenges in photonic systems. Through this work, we illustrated the potential of this method to enable innovative photonic crystal architectures, which can find applications in nonlinear optics, Mach-Zehnder modulators, topological photonics, dispersion engineering for microcombs or quantum optics.

Methods

Inverse design All inverse design problems were set up and optimized with the Spins - inverse design software [40]. For the even mode dispersion engineering we used an in-house version of GPU accelerated Maxwell-B FDFD solver modified to perform eigen-value calculations. For the odd mode and the radiation loss optimization we used Legume, a guided mode expansion software capable of calculating imaginary frequencies incorporating radiative losses [39]. A wrapper for the solver was developed by our team to make this solver compatible with the Spins software. Band calculations in Fig. 2 were done with the in-house iterative GPU-accelerated Mode solver derived from our Maxwell solver. FDTD simulation were performed with Lumerical (Fig. 2). Differences in the way the two simulators discretize on the Yee grid results in a small blue shift comparing the Lumerical results with the Maxwell solver. The band calculation in Fig. 4 which required losses were performed in Legume.

Fabrication The photonic crystal devices were fabricated with silicon-on-insulator wafers with 220 nm silicon and 2 μm of buried oxide. The device patterns were written in ZEP520A in a JEOL JBX-6300FS electron-beam

lithography system. After development the pattern was etched in the silicon layer with a HBr/O₂/He plasma etch. The resist was subsequently removed with an overnight solvent bath and a piranha clean. The buried oxide was removed with buffered oxide etch, BOE, under the PCW, but was left under the grating couplers and strip waveguides. Microposit S1822 resist was used to protect the sample from the etch and openings above the PCWs were patterned in the resist layer using a Durham Magneto Optics ML3 MicroWriter and a development step. After the BOE etch the resist was removed with an overnight solvent bath and a piranha etch.

Transmission measurements Supercontinuum light from a Fianium SC400-4 was coupled into a single mode SMF-28 fiber, which was sent through an in-line fiber optic polarization controller (Thorlabs CPC250), and connected to a stripped and cleaved SMF-28 fiber [41]. The cleaved fiber was positioned above the in-coupling grating couplers using a holder at 5° (from vertical) inclination on a 3-axis piezo stage (Thorlabs NanoMax™ Flexure Stages). Similarly, a cleaved fiber was positioned above the out-coupling grating couplers using a holder at 5° inclination on a 3-axis piezo stage. This output fiber connects to an optical spectral analyser. To isolate the transmission spectrum of the PCW device from the setup and grating coupler losses, we normalized the device measurement to a simple strip waveguide connected to an in- and output grating coupler.

Dispersion measurements The dispersion measurements were performed on a similar grating coupler set as for the transmission setup. The cleaved fibers were replaced by OZ Optics lensed fibers (TSMJ-3A-1550-9/125-0.25-7-2.5-14-2-AR) and the holder was adjusted to a 0° inclination. Instead of the super continuum source, a tunable laser was used, and instead of the OSA we used a detector (Thorlabs DET01CFC). For the

measurements around 1300nm, Santec TSL-510 laser was used in combination with the detector connected to an oscilloscope (Agilent Technologies DSO5054A). For the experiments around 1550nm, the Toptica CLT tunable laser was used combined with the detector, which was connected to the signal analyser of the Toptica Digital Laser Controller.

Back focal plane measurements Detailed description of the back focal plane can be found in the Supplementary Information. Light from a Toptica CLT tunable laser is coupled to a OZ Optics lensed fiber (TPMJ-3A-1300-7/125-0.25-10-2.5-14-1-AR) positioned in a horizontal fiber holder (Thorlabs Fiber Rotator HFR007) on a piezo stage (Thorlabs NanoMax™ Flexure Stages) and used to edge couple light into the sample. A back focal plane microscope is positioned above the sample constructed with a 60X/0.9NA Olympus Plan Fluorite objective and a Alpha NIR InGaAs-camera (Indigo Systems). An aperture in the image plane of the back focal plane microscope is used to select only light emitted by the OPA.

Data availability The data that support the plots within this paper and other findings of this study are available from the corresponding author upon reasonable request.

Acknowledgment This work is funded by the NSF ERFI NewLaw program (Award No. 1741660), and the AFOSR under the MURI program (Award No. FA9550-17-1-0002). The silicon devices were fabricated in the Stanford Nanofabrication Facility and the Stanford Nano Shared Facilities. We also thank Google for providing computational resources on the Google Cloud Platform.

Competing interests. The authors declare they have no competing financial interests.

-
- [1] Soljačić, M. & Joannopoulos, J. D. Enhancement of non-linear effects using photonic crystals. *Nature Materials* **3**, 211–219 (2004).
- [2] Corcoran, B. *et al.* Green light emission in silicon through slow-light enhanced third-harmonic generation in photonic-crystal waveguides. *Nature Photonics* **3**, 206–210 (2009).
- [3] Javadi, A. *et al.* Single-photon non-linear optics with a quantum dot in a waveguide. *Nature Communications* **6**, 6–10 (2015). 1504.06895.
- [4] Marty, G., Combrié, S., Raineri, F. & De Rossi, A. Photonic Crystal Optical Parametric Oscillator. *Nature Photonics* **15**, 53–58 (2021). 2011.13289.
- [5] Zhou, H. *et al.* Enhanced four-wave mixing in graphene-silicon slow-light photonic crystal waveguides. *Applied Physics Letters* **105**, 1–5 (2014).
- [6] Ek, S. *et al.* Slow-light-enhanced gain in active photonic crystal waveguides. *Nature Communications* **5**, 1–8 (2014).
- [7] Nguyen, H. C., Hashimoto, S., Shinkawa, M. & Baba, T. Ultra-compact, low RF power, 10 gb/s silicon Mach-Zehnder modulator. *Optics Express* **20**, 22465–22474 (2012).
- [8] Baba, T. *et al.* Slow-light Mach-Zehnder modulators based on Si photonic crystals. *Science and Technology of Advanced Materials* **15**, 024602 (2014).
- [9] Hinakura, Y., Arai, H. & Baba, T. 64 Gbps Si photonic crystal slow light modulator by electro-optic phase matching. *OECC/PSC 2019 - 24th OptoElectronics and Communications Conference/International Conference Photonics in Switching and Computing 2019* **27**, 14321–14327 (2019).
- [10] Yan, S. *et al.* Slow-light-enhanced energy efficiency for graphene microheaters on silicon photonic crystal wave-

- uides. *Nature Communications* **8**, 1–8 (2017).
- [11] Nozaki, K. *et al.* Sub-femtojoule all-optical switching using a photonic-crystal nanocavity. *Nature Photonics* **4**, 477–483 (2010).
- [12] Qin, K., Hu, S., Retterer, S. T., Kravchenko, I. I. & Weiss, S. M. Slow light Mach–Zehnder interferometer as label-free biosensor with scalable sensitivity. *Optics Letters* **41**, 753 (2016).
- [13] Zhao, Y., Zhang, Y. N. & Wang, Q. High sensitivity gas sensing method based on slow light in photonic crystal waveguide. *Sensors and Actuators, B: Chemical* **173**, 28–31 (2012).
- [14] Wang, B. *et al.* Photonic crystal slot nanobeam slow light waveguides for refractive index sensing. *Applied Physics Letters* **97**, 1–4 (2010).
- [15] Takeuchi, G. *et al.* Thermally controlled Si photonic crystal slow light waveguide beam steering device. *Optics Express* **26**, 11529 (2018).
- [16] Abe, H. *et al.* Two-dimensional beam-steering device using a doubly periodic si photonic-crystal waveguide. *Optics express* **26**, 9389–9397 (2018).
- [17] Ito, H., Tatebe, T., Abe, H. & Baba, T. Wavelength-division multiplexing Si photonic crystal beam steering device for high-throughput parallel sensing. *Optics Express* **26**, 26145 (2018).
- [18] Ito, H. *et al.* Wide beam steering by slow-light waveguide gratings and a prism lens. *Optica* **7**, 47 (2020).
- [19] Dostart, N. *et al.* Serpentine optical phased arrays for scalable integrated photonic lidar beam steering. *Optica* **7**, 726 (2020). 2002.06781.
- [20] Costantini, F. *et al.* Lab-on-chip system combining a microfluidic-ELISA with an array of amorphous silicon photosensors for the detection of celiac disease epitopes. *Sensing and Bio-Sensing Research* **6**, 51–58 (2015).
- [21] Poulton, C. V. *et al.* Long-Range LiDAR and Free-Space Data Communication with High-Performance Optical Phased Arrays. *IEEE Journal of Selected Topics in Quantum Electronics* **25**, 7700108 (2019).
- [22] Raval, M., Poulton, C. V. & Watts, M. R. Unidirectional waveguide grating antennas with uniform emission for optical phased arrays. *Optics Letters* **42**, 2563 (2017).
- [23] Sun, J., Timurdogan, E., Yaacobi, A., Hosseini, E. S. & Watts, M. R. Large-scale nanophotonic phased array. *Nature* **493**, 195–199 (2013).
- [24] Miller, S. A. *et al.* Large-scale optical phased array using a low-power multi-pass silicon photonic platform. *Optica* **7**, 3 (2020).
- [25] Hulme, J. C. *et al.* Fully integrated hybrid silicon two dimensional beam scanner. *Optics Express* **23**, 5861 (2015).
- [26] Acoleyen, K. V., Member, S., Bogaerts, W. & Baets, R. Two-Dimensional Dispersive Off-Chip Beam Scanner. *IEEE Photonics Technology Letters* **23**, 1270–1272 (2011).
- [27] Zhao, Y., Zhang, Y.-N., Wang, Q. & Hu, H. Review on the optimization methods of slow light in photonic crystal waveguide. *IEEE transactions on nanotechnology* **14**, 407–426 (2015).
- [28] Serna, S. *et al.* Experimental gvd engineering in slow light slot photonic crystal waveguides. *Scientific reports* **6**, 26956 (2016).
- [29] Rahimi, S., Hosseini, A., Xu, X., Subbaraman, H. & Chen, R. T. Group-index independent coupling to band engineered SOI photonic crystal waveguide with large slow-down factor. *Optics Express* **19**, 21832 (2011).
- [30] Molesky, S. *et al.* Inverse design in nanophotonics. *Nature Photonics* **12**, 659–670 (2018).
- [31] Burger, M., Osher, S. J. & Yablonovitch, E. Inverse problem techniques for the design of photonic crystals. *IEICE transactions on electronics* **87**, 258–265 (2004).
- [32] Preble, S., Lipson, M. & Lipson, H. Two-dimensional photonic crystals designed by evolutionary algorithms. *Applied Physics Letters* **86**, 1–3 (2005).
- [33] Riishede, J. & Sigmund, O. Inverse design of dispersion compensating optical fiber using topology optimization. *Journal of the Optical Society of America B* **25**, 88 (2008).
- [34] Wang, F., Jensen, J. S. & Sigmund, O. Robust topology optimization of photonic crystal waveguides with tailored dispersion properties. *Journal of the Optical Society of America B* **28**, 387–397 (2011).
- [35] Matzen, R., Jensen, J. S. & Sigmund, O. Systematic design of slow-light photonic waveguides. *Journal of the Optical Society of America B* **28**, 2374 (2011).
- [36] Vercruyssen, D., Sapra, N. V., Su, L. & Vu, J. Dispersion Engineering with Photonic Inverse Design. *Ieee Journal Of Selected Topics In Quantum Electronics* **26**, 8301706 (2020).
- [37] Zhai, Y., Tian, H. & Ji, Y. Slow light property improvement and optical buffer capability in ring-shape-hole photonic crystal waveguide. *Journal of Lightwave Technology* **29**, 3083–3090 (2011).
- [38] Vercruyssen, D., Sapra, N. V., Su, L., Trivedi, R. & Vučković, J. Analytical level set fabrication constraints for inverse design. *Scientific Reports* **9**, 1–7 (2019).
- [39] Minkov, M. *et al.* Inverse design of photonic crystals through automatic differentiation. *ACS Photonics* **7**, 1729–1741 (2020).
- [40] Su, L. *et al.* Nanophotonic inverse design with spins: Software architecture and practical considerations. *Applied Physics Reviews* **7**, 011407 (2020).
- [41] Sapra, N. V. *et al.* Inverse Design and Demonstration of Broadband Grating Couplers. *IEEE Journal of Selected Topics in Quantum Electronics* **25** (2019).